POLITECNICO DI TORINO
Repository ISTITUZIONALE

Exploratory Acoustic Investigation of Customizable 3D-Printed Hybrid Acoustic Materials (HAMs) through Interlaboratory Impedance Tube Measurements

Original
Exploratory Acoustic Investigation of Customizable 3D-Printed Hybrid Acoustic Materials (HAMs) through Interlaboratory Impedance Tube Measurements / Tsiokou, Vaia; Shtrepi, Louena; Badino, Elena; Astolfi, Arianna; Karatza, Anna. - In: ACOUSTICS. - ISSN 2624-599X. - 5:3(2023), pp. 653-675. [10.3390/acoustics5030040]

Availability:
This version is available at: 11583/2980389 since: 2023-07-16T17:00:25Z

Publisher:
Basel: MDPI 2003

Published
DOI:10.3390/acoustics5030040

Terms of use:

This article is made available under terms and conditions as specified in the corresponding bibliographic description in the repository

Publisher copyright

(Article begins on next page)

29 April 2024

acoustics

MDPI

Article

Exploratory Acoustic Investigation of Customizable 3D-Printed Hybrid Acoustic Materials (HAMs) through Interlaboratory Impedance Tube Measurements

Vaia Tsiokou [1], Louena Shtrepi [2,*], Elena Badino [2], Arianna Astolfi [2] and Anna Karatza [1]

[1] BioG3D P.C., LTCP, Lavriou Avenue 1, 19500 Lavrion, Greece; vtsiokou@biog3d.gr (V.T.); akaratza@biog3d.gr (A.K.)
[2] Department of Energy, Politecnico di Torino, Corso Duca degli Abruzzi 24, 10129 Torino, Italy; elena.badino@polito.it (E.B.); arianna.astolfi@polito.it (A.A.)
* Correspondence: louena.shtrepi@polito.it

Abstract: Acoustic materials are widely used for improving interior acoustics based on their sound absorptive or sound diffusive properties. However, common acoustic materials only offer limited options for customizable geometrical features, performance, and aesthetics. This paper focuses on the sound absorption performance of highly customizable 3D-printed Hybrid Acoustic Materials (HAMs) by means of parametric stepped thickness, which is used for sound absorption and diffusion. HAMs were parametrically designed and produced using computational design, 3D-printing technology, and feedstock material with adjustable porosity, allowing for the advanced control of acoustic performance through geometry-related sound absorbing/diffusing strategies. The proposed design methodology paves the way to a customizable large-scale cumulative acoustic performance by varying the parametric stepped thickness. The present study explores the challenges posed by the testing of the sound absorption performance of HAMs in an impedance tube. The representativeness of the test samples (i.e., cylindrical sections) with respect to the original (i.e., rectangular) panel samples is contextually limited by the respective impedance tube's geometrical features (i.e., cylindrical cross-section) and dimensional requirements (i.e., diameter size). To this aim, an interlaboratory comparison was carried out by testing the normal incidence sound absorption of ten samples in two independent laboratories with two different impedance tubes. The results obtained demonstrate a good level of agreement, with HAMs performing better at lower frequencies than expected and behaving like Helmholtz absorbers, as well as demonstrating a frequency shift pattern related to superficial geometric features.

Keywords: architectural acoustics; Hybrid Acoustic Materials (HAMs); sound absorption; computational design; 3D printing; interlaboratory comparison; impedance tube

check for updates

Citation: Tsiokou, V.; Shtrepi, L.; Badino, E.; Astolfi, A.; Karatza, A. Exploratory Acoustic Investigation of Customizable 3D-Printed Hybrid Acoustic Materials (HAMs) through Interlaboratory Impedance Tube Measurements. *Acoustics* **2023**, *5*, 653–675. https://doi.org/10.3390/acoustics5030040

Academic Editor: José Sánchez-Dehesa

Received: 9 March 2023
Revised: 6 July 2023
Accepted: 10 July 2023
Published: 13 July 2023

Copyright: © 2023 by the authors. Licensee MDPI, Basel, Switzerland. This article is an open access article distributed under the terms and conditions of the Creative Commons Attribution (CC BY) license (https://creativecommons.org/licenses/by/4.0/).

1. Introduction

Acoustics is a crucial factor for human comfort and well-being in any built environment. Sound can be considered as important as any other architectural aspect that contributes to spatial quality and can be shaped through design principles. Through the parametrization of boundary surfaces, geometric features, and material properties, the individual acoustic experience related to the functions hosted in an interior space can be highly customizable [1]. However, state-of-the-art measurement methods need to be further tested and validated for innovative structures. The aim of this paper is to address some of the challenges in the characterization of the acoustic properties of customizable 3D-printed materials. The focus is on sound absorption property characterization through the measurements of two different impedance tubes.

Indoor acoustics are highly affected by the choice of materials and geometrical configurations [2]. Studies show that millions of citizens within the WHO European Region

spend approximately 90% of their time in indoor spaces: their homes (2/3 of this time) and workplaces, schools, and public spaces (1/3 of this time) [3]. Considering that Europe has a significant proportion (90%) of buildings constructed before 1990 and a 40% proportion constructed before 1960, the issue of acoustic management, human comfort, and well-being is brought to the forefront [4]. In this frame, a huge opportunity for the improvement in the acoustic quality of indoor spaces arises, paving the way for innovative, sustainable, and customizable solutions for acoustic renovation in order to meet current standard regulations. With mass customization as the inherent aspect of Additive Manufacturing (AM) [5], designers are now much more able to positively influence both outdoor and indoor acoustics towards these new frontiers.

The use of AM to produce acoustic materials has been increasingly studied in the last few years. In terms of building acoustics, recent studies have focused on the large-scale 3D printing of full-scale building elements (e.g., wall panels) that combine both thermal and sound-insulating properties [6–8]. On a smaller scale, the development of 3D-printed sound-absorbing materials has been increasingly explored in several studies, including sound absorbers with controlled porosity [9–11], microperforated panels [12], and metamaterials [13]. Moreover, 3D-printed panels have also been combined with porous sound absorbers to enhance the performances of the latter [12,14,15]. The production of porous sound-absorbing materials with AM is a promising approach to control the pores' shape and network, within a lattice structure, and optimize their tortuosity and porosity. The intended acoustic performances have been targeted through a variety of 3D-printing technologies, materials, and design principles.

Open-porous Acrylonitrile Butadiene Styrene (ABS) lattice structures have been previously 3D printed through Fused Deposition Modeling (FDM), suggesting that their sound-absorbing performance is highly influenced by their thickness [9]. A metafluid bio-inspired cereal straw has been fabricated through the Fused Filament Fabrication of thermoplastic to form a periodic repetition of double Quarter-Wavelength Resonators (QWR) [16]. Resin-based acoustic metamaterials based on Helmholtz resonators have also been produced through Stereo-Lithography (SLA), where the addition of a thin 3D-printed membrane at the base of the resonators aims to enhance the stop band [17]. In addition, sound absorbers based on the principle of Passive Destructive Interference (PDI) have been fabricated through powder-based Polyamide Selective Laser Sintering (SLS). The scope of these compact-size resonators was tailored, in terms of extended absorption bandwidth, through targeted performance-driven combinations and with the addition of a resistive layer at the orifices for site-specific applications [18,19]. Micro-Perforated Panels (MPP) operating on the principle of Helmholtz resonators (i.e., when excited by a sound wave, the mass of air in the holes oscillates in front of the elastic air volume) have also been produced through FDM, employing Polylactic acid/Polyhydroxyalkanoates-Wood Fiber (PLA/PHAWF) composites [20], powder-based Selective Laser Sintering (SLS) [21], and MultiJet Printing (MJP) [22], suggesting a correlation between the sound absorption performance and the material porosity in terms of micro-tube design features. Furthermore, gypsum-based 3D-printed porous metamaterials with various open-cell structures and porosity have been investigated [23]. The specimens produced through Binder Jetting (BJ) technology were analyzed considering the effect of the unit-cell structure. The results indicated an increased sound absorption capacity performance for Octet lattice and Gyroid structures.

In order to measure the sound absorption performances of the 3D-printed panels, in most past studies, the normal incidence sound absorption coefficient of different 3D-printed porous sound absorbers was measured in an impedance tube [9,13,15,23–25] or predicted through theoretical models [12,13,15,23].

Given the novelty of porous 3D-printed materials with respect to traditional ones, past researchers studied the extent to which the measured sound absorption coefficient of a given sample is influenced by the 3D-printing techniques used for its production [25], i.e., the impedance tube characteristics and the presence of air gaps at the back of the

sample [9,11,25]. In particular, the work in [25] presented a Round Robin test on the influence of different AM technologies (e.g., FFF, SLS, SLM, and LCD), materials (e.g., PLA, ABS, polyamide or aluminum powder, and photopolymer resin), and 3D-printing devices on the measured sound absorbing performance of porous samples exhibiting two different cellular designs. The measurements were conducted by independent laboratories with impedance tubes of different diameters. The study highlighted that while most of the measurement results were very close, some discrepancies were reported due to (a) shape and surface imperfections, or microporosity, induced by the manufacturing process; (b) imperfect matching between the tube and sample diameter; and (c) different geometric details present at the circular edges of the samples, based on the cellular design and sample diameter.

While previous studies focused on porous sound-absorbing materials composed of a 3D-printed lattice micro-geometry of single thicknesses, to the best knowledge of the authors, no previous investigation was found on 3D-printed materials combing sound-absorbing and diffusing properties. Such materials, commonly known as "hybrid" materials, can be created by combining a porous layer designed for absorption with surface irregularities that promote sound diffusion [26]. In the present exploratory study, the presence of surface irregularities in the form of variable patterned stepped thickness poses new challenges to the characterization of the sound-absorbing performance of such materials in the impedance tube. Indeed, the representativeness of the test samples (i.e., cylindrical sections) with respect to the original (i.e., rectangular) panel samples is limited by the impedance tube's geometrical features and dimensional requirements (i.e., cylindrical cross-section and respective diameter size). Therefore, the cylindrical samples selected for representation are required to exhibit the essential characteristics of the entire rectangular area's irregular surface pattern.

This contribution focuses on the sound-absorbing performance of 3D-printed HAMs and explores the challenges associated with their characterization in the impedance tube, considering the need to adequately represent the surface irregularities within the aforementioned geometrical and dimensional constraints of an impedance tube. To this aim, two different measurement set-ups (of cylindrical cross-sections, but with different diameters) were used to measure the sound absorption capacity of ten different material typologies, according to EN ISO/IEC 17025:2017 [27]. The intent of the present work is to add to the previous scientific knowledge acquired through interlaboratory testing on the sound absorptive properties of 3D-printed open-cell specimens of a single thickness [25], with the introduction of an innovative design variable of parametric stepped thickness. To the best of the authors' knowledge, this key parameter, enabled through computational design and 3D printing, has not been previously investigated. Therefore, the main objectives of the present work are summarized as follows:

An interlaboratory [27] comparison of ISO 10534-2:2001 [28] measurements with two different impedance tubes.

An exploratory study on the effect of the sample diameter [25] and sample typology [9], highlighting the effect of surface irregularities in the form of variable patterned stepped thickness, for future targeted compilations [18–20].

A consideration of the 3D-printed gyroid cellular core design [23,25] acoustic properties made of a customizable lightweight thermoplastic material (i.e., PLA) [20].

However, the analysis of the diffusing properties of these typologies is out of the scope of the present study.

2. Methodologies

2.1. Design and Theoretical Bases

In the present study, a new class of HAMs with absorption in lower frequencies was proposed by manipulating their surfaces and overall thicknesses. This was pursued by means of an irregular stepped pattern based on Truchet tiling [29] and a gyroid macroporous structure with a proven absorbing capacity [23]. The Truchet tiling concept was

selected as a means to develop an infinite and modular non-repeating pattern, appropriate for extended architectural surfaces.

The basic concept relies on and takes inspiration from the Schroeder diffuser design which is often interpreted as being a surface with a spatially-varying impedance [26]. In the proposed design, the variable impedance was achieved by patches of absorption and reflection combined in a complex 3D quarter-circle Truchet design. The aim was to build a hybrid surface which is the result between a pure 3D-printed porous absorber and a diffuser. Partial absorption was considered inherent in the design while any reflected sound is dispersed. The porous absorber, i.e., 3D-printed foam, was faced with a complex mask that allows the creation of laterally slotted panels with rectangular vertically oriented slits that follow the quarter-circle Truchet design. As in hybrid surfaces based on the same principle, it was expected that the additional vibrating mass within the open areas of the mask would shift the absorption curve down in frequency, generating additional low- to mid-frequency absorption. At high frequencies, the hard parts of the mask reflected sound, causing a reduction in the absorption coefficient [26]. It is at these high frequencies, where the absorption is reduced, that the surface disperses the reflected sound. Cox and D'Antonio [26] presented the bases of the discussion of the design of hybrid surfaces' diffuse properties using the simplest Fourier theory. They highlighted that this simple prediction theory and the subsequent design process are only applicable at mid- and high-frequency, while at low frequency the mutual interactions across the surface make the prediction model inaccurate. As mentioned in the previous section, the dispersed sound has not been investigated in this work.

Regarding the absorbed sound, an approximation to the model of the slotted absorbers, which are a derivation of the Helmholtz absorbers, was assumed. A simple model was also implemented in [30] based on the theory developed in [26]. The model required data on airflow resistivity, top coating thickness, slot width, porous material thickness, and open area. Given that no airflow resistivity measurements could be performed in the framework of this study, more exact theories to match the experimental results could not be implemented. Therefore, it was not considered further in the present work which relies on exploratory experimental work.

Ten hybrid acoustic panel typologies were designed in the integrated development platform Grasshopper for Rhino 7. The panels consisted of a porous lattice structure, i.e., a foam core as a cellular porous material, which provides sound absorption, covered by a cut-out sound reflective layer with different surface patterns, which provides sound diffusion while enabling the sound energy to access the porous layer through the lateral sides. A pattern consisting of quarter-circle Truchet tiles (Figure 1), connecting the midpoints of adjacent sides was employed for the upper surface pattern.

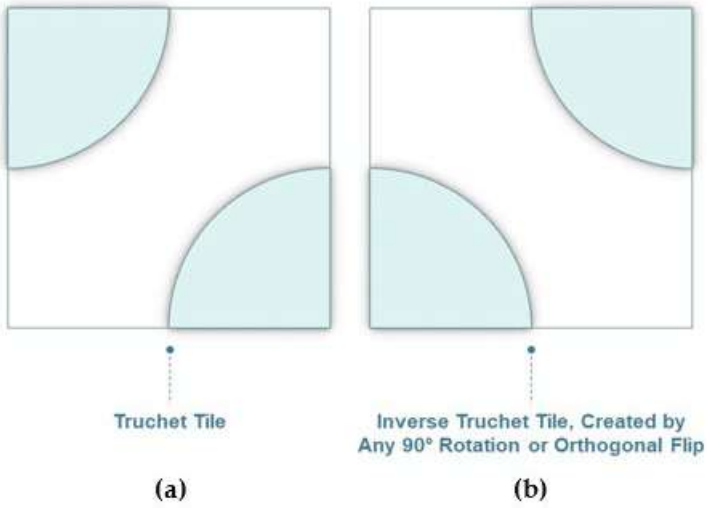

Figure 1. Truchet tiling: (**a**) principal 2D quarter-circles; (**b**) 90° rotation of principal 2D quarter-circles.

The Z coordinates of points on the 2D quarter-circles were remapped to form a parametric stepped profile curve on the X–Z plane. The parameters for the formation of the profile curve were the number of steps (i.e., 1 to 3 steps) and the controllable curvature through a Bézier curve graph mapper (Figure 2a). This profile curve defined the boundary conditions of regular and irregular polygons (Figure 2b) for a dual-material properties allocation during the realization of the design. In the following sections, the two intended material functionalities (i.e., foam core and high-density surface) are represented in white and cyan colors, respectively. The polygons were then revolved and mirrored to form the principal 3D quarter-circle Truchet tile (Figure 2c). Each such tile was randomly repeated within a rectangular 2D grid (L160 mm × W160 mm) (Figure 2d)) in two different orientations: the principal Truchet tile orientation and its inverse, created by any 90° rotation or orthogonal flip (Figure 2e).

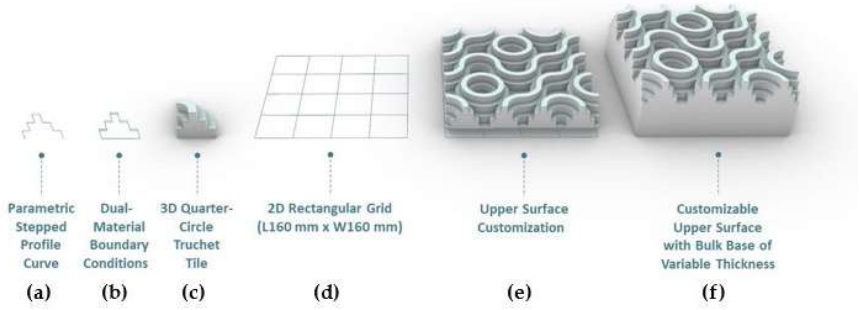

Figure 2. Design methodology for hybrid indoor acoustic panels with a customizable upper surface and variable thickness: (**a**) parametric stepped profile curve with a variable number of steps; (**b**) dual-material boundary conditions; (**c**) 3D quarter-circle Truchet tile; (**d**) 2D rectangular grid (L160 mm × W160 mm), (**e**) upper surface customization; and (**f**) customizable upper surface with a bulk base of variable thickness.

Five typologies of the upper surface of the acoustic panels (i.e., A, B, C, D, and E) were generated by tuning the Truchet tile size (i.e., 20 mm for B and D and 40 mm for A, C, and E) on the grid, as well as the aforementioned parameters for the quarter-circle profile curve (i.e., number of steps ranging from 1 to 3 and Bézier curve). Finally, the five upper surface typologies were applied over bulk bases to generate hybrid acoustic panels (Figure 2f). The employed bulk bases are of two thicknesses, i.e., 70 mm and 50 mm, respectively, referred to in the identification code of the panels with numbers 1 and 2, allowing for the formation of ten acoustic panel typologies in total, classified as A1, A2, B1, B2, etc. (Figure 3).

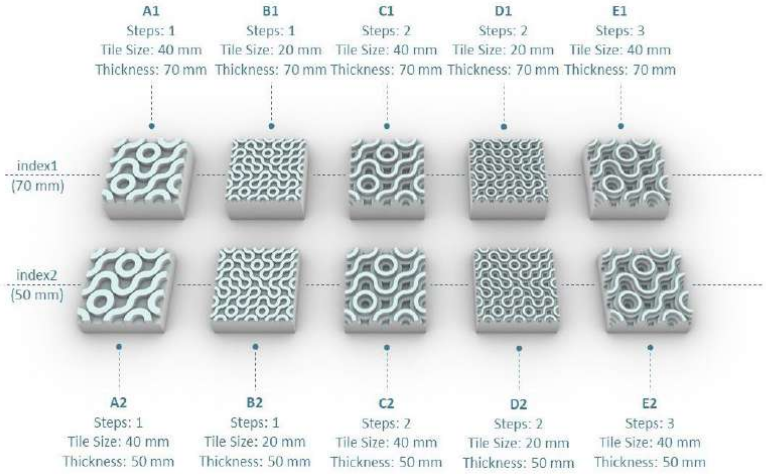

Figure 3. Ten hybrid indoor acoustic panel typologies with a customizable upper surface and variable thickness.

As indicated in the following section (i.e., Section 2.2), the bulk bases were further customized in terms of macro-porosity, through a gyroid pattern (Figure 4), in order to create the foam-cores. The designed pore size and porosity are estimated 5 mm and 80%, respectively [31].

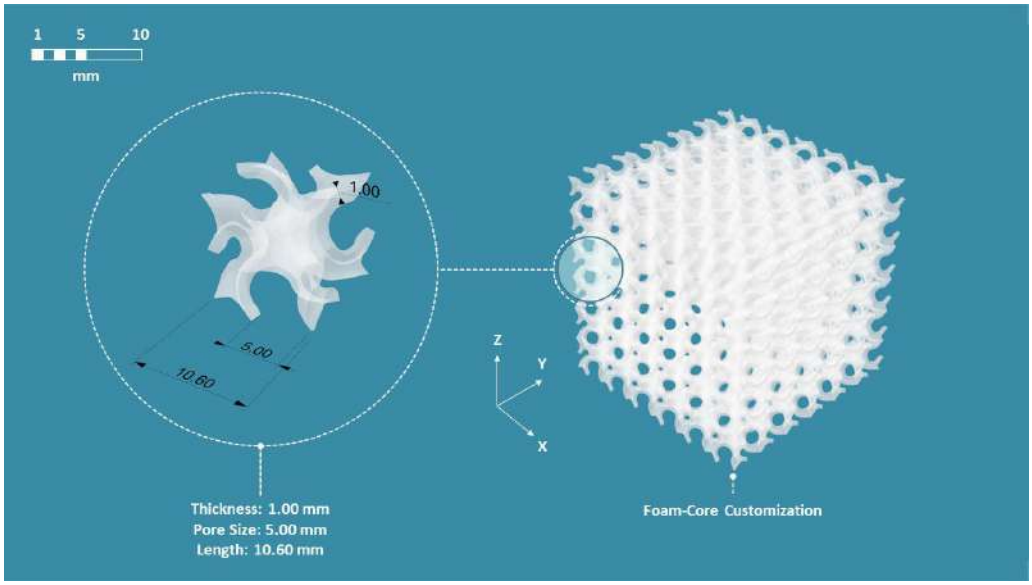

Figure 4. Customization of the foam-core macro-porosity through a gyroid pattern.

2.2. Materials and Fabrication

The testing specimens were fabricated in a dual-nozzle Raise3D Pro2 Plus FFF unit, employing the commercial thermoplastic filament (Ø1.75 mm) colorFabb Light-Weight PLA (LW PLA) Natural (colorFabb, Belfeld, The Netherlands) and capitalizing on its customizable functionality. The complete property range of LW-PLA is analyzed in Table A1 (see Appendix A) [32]. The specified material contains foaming agents that become activated at around 230 °C, thus, allowing fine-tuning of the extruded material's volume by regulating the printing temperature along other parameters. The same material was 3D printed by employing two different profiles with respect to its location, i.e., foam core and top cut-out surfaces. Both 3D-printing profiles were created in the 3D Slicer Software ideaMaker 4.3.1. Printing Profile A (i.e., the left extruder with a temperature set at 265 °C, allowing for the agents' activation) for the foam core, while Printing Profile B (i.e., the right extruder's temperature set at 207 °C) was employed for the top cut-out surfaces. The core of all specimens was printed as an open-cell structure based on a gyroid pattern of 20% density (Printing Profile A). The bottom of the foam cores was created with solid fill layers following a linear pattern (alternately 45° and 135° per layer). Finally, the upper surfaces were printed as a compact layer (infill pattern of 100% density) of 2 mm thickness (Printing Profile B). The detailed slicing parameters for the 3D printing procedure are presented in Table 1.

In order to carry out the acoustic performance testing of the 10 panels, the cylindrical specimen cut-outs for each panel typology were printed with two diameters (i.e., Ø60 mm and Ø35 mm) and two thicknesses (i.e., 70 mm and 50 mm).

Figure 5 demonstrates the allocation of the variant material properties in the two specimen sets (i.e., 60 mm samples and 35 mm samples) according to the two slicing profiles. Printing Profile A is represented in both samples in white color, whereas Printing Profile B is represented in cyan color.

Table 1. The 3D printing profiles for the realization of the samples using dual-nozzle printing for the integration of two functionalities.

	Printing Profile A	**Printing Profile B**
First Layer Height	0.10 mm	-
Layer Height	0.20 mm	0.20 mm
Extrusion Width	0.75 mm	0.60 mm
Shells	0	0
Retraction Speed	45 mm/s	45 mm/s
Retraction Material Amount	0.50 mm	0.50 mm
Flowrate	45%	90%
Infill Pattern Type	Gyroid	Grid
Infill Density	20%	100%
First Layer Solid Fill Pattern	Lines	-
Bottom Solid Fill Layers	2	-
Bed Temperature	60 °C	60 °C
Extruder	**265 °C**	**207 °C**
Fan Speed	No Fan	No Fan
First Layer Speed	15.00 mm/s	-
Default Printing Speed	40 mm/s	40 mm/s

The specified material contains foaming agents that become activated at around 230 °C, thus, allowing fine-tuning of the extruded material's volume by regulating the printing temperature along other parameters. The same material was 3D printed by employing two different profiles with respect to its location, i.e., foam core and top cut-out surfaces.

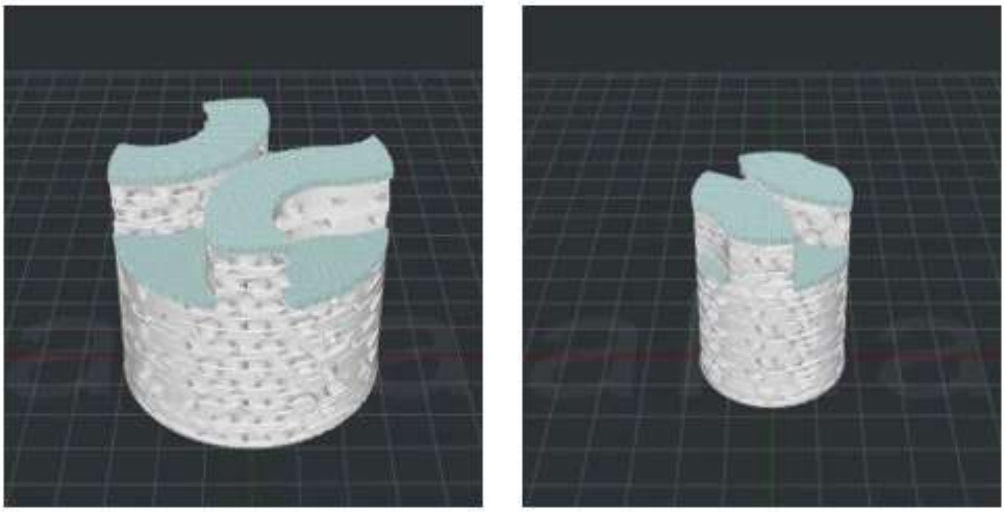

Figure 5. Allocation of the variant material properties based on Printing Profile A and Printing Profile B in the two indicative specimen sets: (**a**) 60 mm samples; (**b**) 35 mm samples.

2.3. Tested Configurations

For the needs of the acoustic analysis, representative circular areas of the upper surface typologies were selected (Figure 6) to produce the 60 mm samples and 35 mm samples. The areas of the upper surface were randomly opted, ensuring the inclusion of all steps involved in each typology.

More detailed information on the geometry and dimensions of the different sample typologies are reported in the following. The number of steps, step size, and remaining core thickness (i.e., measured height from the bottom level up to the level where the surface pattern begins) of the samples are presented in Table 2.

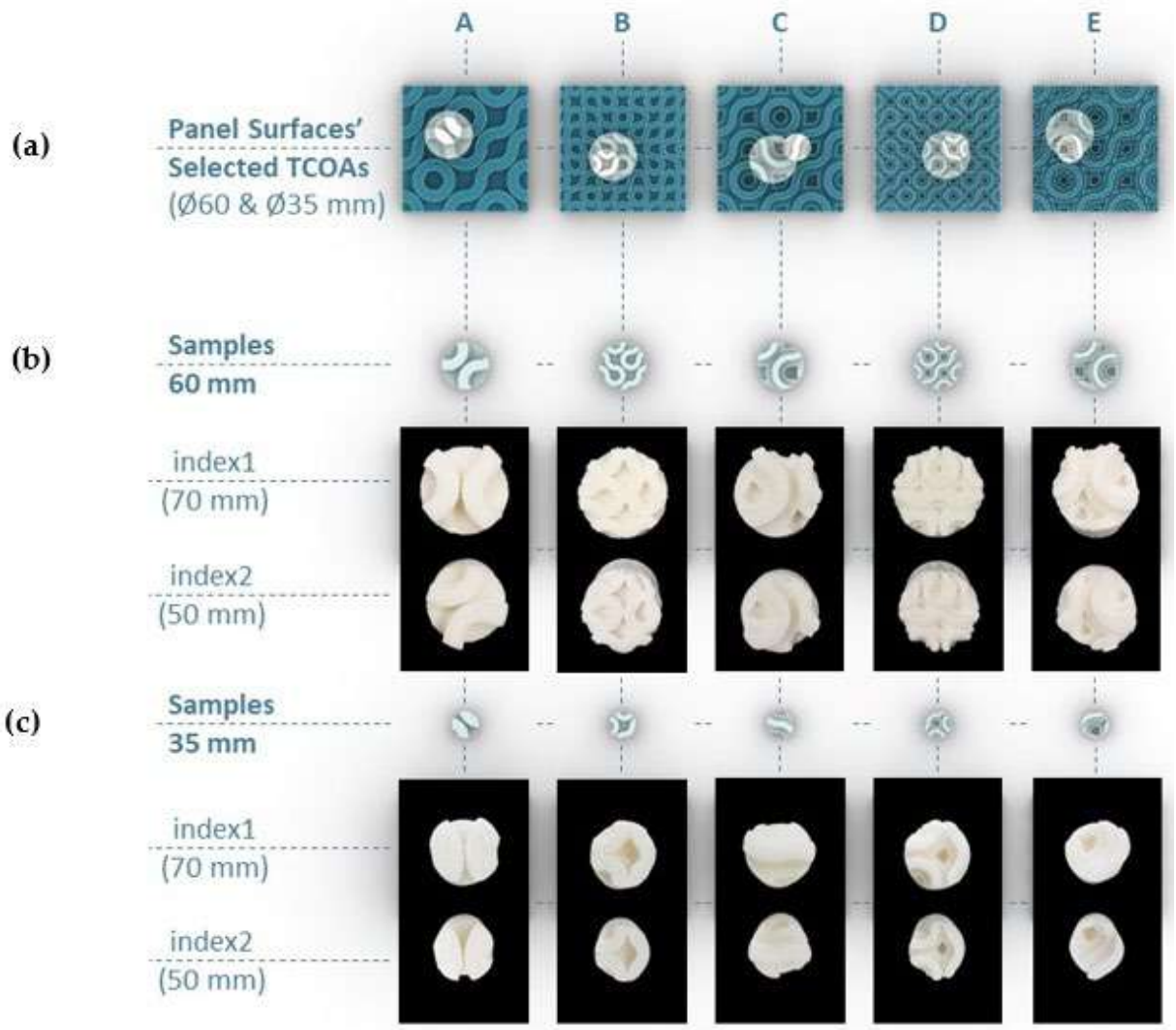

Figure 6. Selected TCOAs: (**a**) circular TCOAs for the 60 mm samples and 35 mm sampled in relation to rectangular panels' TCOAs; (**b**) 60 mm samples; and (**c**) 35 mm samples.

Table 2. Step size, number of steps, and remaining core thickness of the sample typologies for both 60 mm samples and 35 mm samples.

Sample Typology	Number of Steps	Step Size (mm)	Remaining Core Thickness (mm)
A1	1	13.3	54.7
B1	1	6.7	61.3
C1	2	10.7	46.7
D1	2	5.3	57.3
E1	3	8.6	42.3
A2	1	13.3	34.7
B2	1	6.7	41.3
C2	2	10.7	26.7
D2	2	5.3	37.3
E2	3	8.6	22.3

While, for reference, the volumes (with a material density of 230 kg/m^3) of the two sample sets, (i.e., with 60 mm and 35 mm diameters), with core thickness and respective steps included, are collected in Table 3.

Table 3. Volumes of A, C, and E typologies for both 60 mm samples and 35 mm samples.

Sample Typology	Volume ($\times 10^{-5}$ m^3) of 60 mm Samples	Volume ($\times 10^{-5}$ m^3) of 35 mm Samples
A1	17.3	5.98
B1	18.4	6.10
C1	16.6	5.52
D1	18.0	5.98
E1	16.2	5.22
A2	11.6	4.11
B2	12.7	4.23
C2	10.9	3.65
D2	12.4	4.11
E2	10.5	3.35

For each specimen in the two sets, both the Top Cut-Out Areas (TCOAs) and the Lateral Cut-Out Areas (LCOAs) were calculated (Figure 7). The TCOAs were defined as the horizontally planar Truchet surfaces (i.e., the *goings* of all the steps, in terms of stair design terminology) and LCOAs were defined as the vertically developed Truchet surfaces (i.e., the *rises* of all the steps, in terms of stair design terminology).

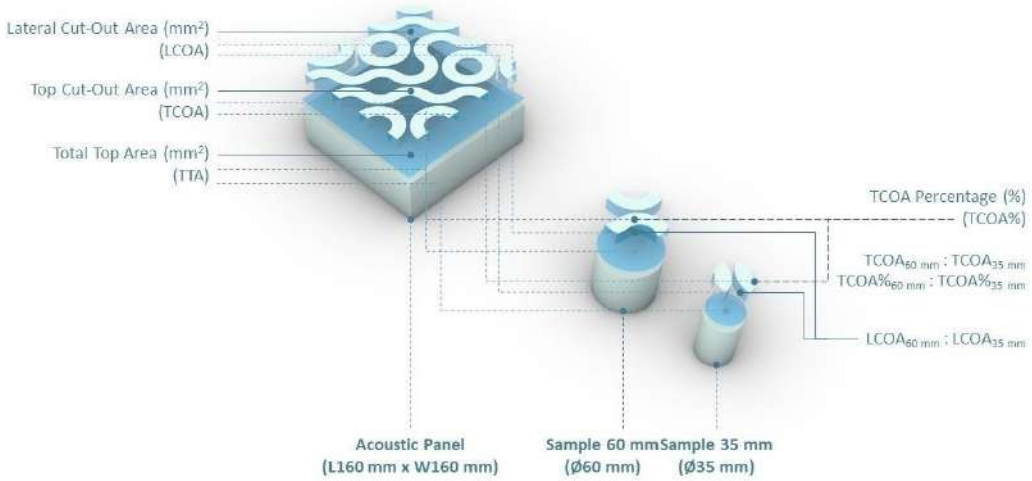

Figure 7. The TCOAs, LCOAs, and TTAs on rectangular acoustic panels, 60 mm samples, and 35 mm samples. The $TCOAs_{60\ mm}$ and $TCOAs_{35\ mm}$ evaluated as a percentage with respect to the TTA of the respective cylindrical specimens.

The specimens' TCOAs were evaluated as percentages in relation to the total TCOAs of the respective rectangular panel surfaces. Furthermore, the frequency of occurrence for the selected TCOAs within the rectangular areas was taken into consideration (Table 4). The aggregated areas were then calculated as representative percentages of measurement coverage (Figure 8b,c).

Table 4. The frequency of occurrence for the 60 mm samples and 35 mm samples within the respective rectangular panel surfaces.

	60 mm Samples	35 mm Samples
A	2	16
B	1	17
C	2	6
D	2	17
E	2	2

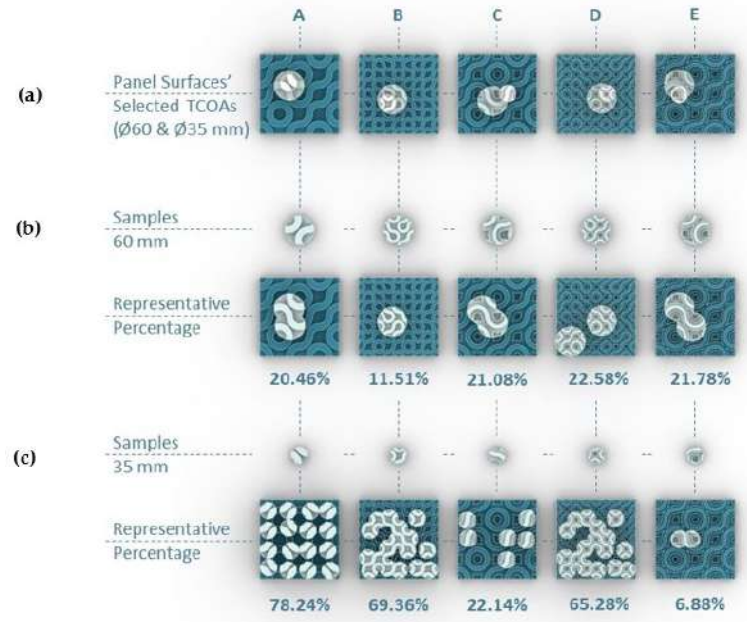

Figure 8. Selected TCOAs and their frequency of occurrence: (**a**) circular TCOAs for 60 mm samples and 35 mm samples in relation to the rectangular panels' TCOAs; (**b**) 60 mm samples and their representative percentage of measurement coverage based on their frequency of occurrence; (**c**) 35 mm samples and their representative percentage of measurement coverage based on their frequency of occurrence.

The TCOAs were also evaluated as a percentage in relation to the Total Top Area (TTA) of the respective cylindrical specimens (referred to as TCOA%). Finally, the TCOA Ratios ($TCOA_{60\ mm}$: $TCOA_{35\ mm}$), as well as the TCOA% Ratios ($TCOA\%_{60\ mm}$: $TCOA\%_{35\ mm}$) and the LCOA Ratios ($LCOA_{60\ mm}$: $LCOA_{35\ mm}$), were calculated. The scope of these interdependencies was to identify similarities or differences in the percentage values of TCOAs with respect to the TTAs of both the 60 mm samples and the 35 mm samples. A mean TCOA% Ratio of ∼1.00 (i.e., 0.92) indicated closeness in the percentage values. This essentially means that even though the TCOAs are larger in the 60 mm samples, the percentage of the area that was cut out in relation to the total circular area (in both 60 mm samples and 35 mm samples) is almost equal, and this could indicate similarities in the results. Tables 5 and A2 (see Appendix B) represent an analysis of the interdependent data for the five surface design typologies (i.e., A, B, C, D, and E).

Table 5. Aggregated data on TCOA Ratios ($TCOA_{60\ mm}$: $TCOA_{35\ mm}$), TCOA% Ratios ($TCOA\%_{60\ mm}$: $TCOA\%_{35\ mm}$), and LCOA Ratios ($LCOA_{60\ mm}$: $LCOA_{35\ mm}$).

Samples	TCOA Ratios ($TCOA_{60\ mm}$: $TCOA_{35\ mm}$)	TCOA% Ratios ($TCOA\%_{60\ mm}$: $TCOA\%_{35\ mm}$)	LCOA Ratios ($LCOA_{60\ mm}$: $LCOA_{35\ mm}$)
A1	2.09	0.69	2.24
A2	2.09	0.69	2.24
B1	2.82	0.93	2.86
B2	2.82	0.93	2.86
C1	2.86	0.95	2.90
C2	2.86	0.95	2.90
D1	2.94	0.97	3.08
D2	2.94	0.97	3.08
E1	3.17	1.05	3.00
E2	3.17	1.05	3.00
Mean	2.78	0.92	2.82

Furthermore, the open area was calculated as the ratio of LCOA and the total irregular surface area (LCOA + TCOA). It has been observed that the open areas are comparable for the two series of samples (i.e., 60 mm samples and 35 mm samples) (see Appendix B, Table A2) [26,30].

2.4. Acoustic Characterization

The sound absorption coefficient (α) was used to characterize the different samples. It is defined as the ratio of the energy absorbed by a surface to the energy incident. The absorption coefficient can be defined for a specific angle of incidence or random incidence [26]. Measurements have been performed in the impedance tube in accordance with ISO 10534-2:2001 [28] (two-microphone technique) in order to measure the normal-incidence absorption coefficient (α_0).

This method relies on measurements obtained from small samples suitable to the aim of the interlaboratory comparison (i.e., in consideration of the dimensional constraints and representativeness of surface irregularities with respect to the entire rectangular area's irregular surface pattern) [27]. The measurements took place in BIOG3D (Lavrion Technological Cultural Park—LTCP) and the Applied Acoustics Laboratory (Department of Energy, Politecnico di Torino). Two different impedance tubes were used: a custom impedance tube, equipped with two MPA416 1/4" microphones (BSWA Tech, Beijing, China) (identified in the following as "IT_{60}"), and an HW-ACT-TUBE (Siemens, Munich, Germany), equipped with two 1/4" flush-mounted GRAS 46BD (GRAS, Holte, Denmark) microphones (identified in the following as "IT_{35}"). Both impedance tube configurations consisted of a loudspeaker, a sound propagation tube, microphone holders, and sample tubes with a diameter of 60 mm and 35 mm. In general, the method allows for accurate sound pressure amplitude and phase measurements in the whole frequency range of interest, i.e., 100–5000 Hz [28]. In our experimental study, the geometry of the tubes follows the specifications of ISO standards, including the minimum distance between the microphone and source, and the microphone and test sample. In particular, IT_{60} has been equipped with two microphone holders, with a fixed microphone spacing of 45 mm, allowing for measurements at a frequency range from 125 to 3150 Hz. IT_{35} has been equipped with three microphone holders to extend the supported frequency range as much as possible. Therefore, it is possible to obtain accurate measurements at a low-frequency range of 50 to 2400 Hz and a high-frequency range of 119 to 5700 Hz when 65 mm and a 29 mm microphone spacing are used, respectively. The latter distance has been used for the aim of this work. For the sake of clarity, the measurement results of both impedance tubes are reported for the frequency range between 125 and 3150 Hz (see Section 3).

The air temperature, relative humidity, and atmospheric pressure were monitored with properly calibrated transducers during the measurement campaigns. The test specimens were mounted at the end of the respective impedance tubes by means of sample holders, which were assumed to behave as a rigid termination, with no gaps between the samples and the termination.

The experimental campaign was preceded by a comparison between the two tubes in order to investigate any possible artifacts. The comparison of the sound absorption coefficients was performed on a baseline porous material made of polyester fiber with a density of 29 kg/m^3 and a thickness of 85 mm. Moreover, given the presence of surface irregularities on the samples, as a preliminary and complementary step, the potential effect of the samples' orientation within the tube on the measured sound absorption coefficient was evaluated (see Appendix C). A deeper investigation was performed on one of the randomly chosen samples (C2) to assess the effect of the top cut-out surfaces and foam core. To this aim the original sample C2 was progressively sectioned by using a coping saw (see Appendix D).

Nonetheless, the interlaboratory testing presented is primarily focused on the effect of the sample diameter (see Section 3.2) and sample typology (see Section 3.3).

Due to 3D printing limitations, all measurements were performed on single samples for each typology; thus, it was not possible to assess reproducibility contributions. Repeatability was evaluated by repeating the measurement three times for each typology in both tubes without varying the set-up conditions (e.g., re-mounting the sample). The results showed highly repeatable measurements with maximum standard deviations (SD_{max}) of 0.002. Due to the limited visual presentation of such small values, these were not presented in the graphs. For both measurements, the sound absorption coefficient (α_0) was determined with a resolution of 2 Hz and represented in one-third-octave bands.

3. Results and Discussion

3.1. Baseline Material Comparisons

The results of the preliminary investigation on the influence of the two tubes on the baseline material measurement results are shown in Figure 9b. It can be observed that the differences are very small, and the results could be considered compatible. Therefore, it could be considered that the differences observed in the following sections are due to the sample properties only.

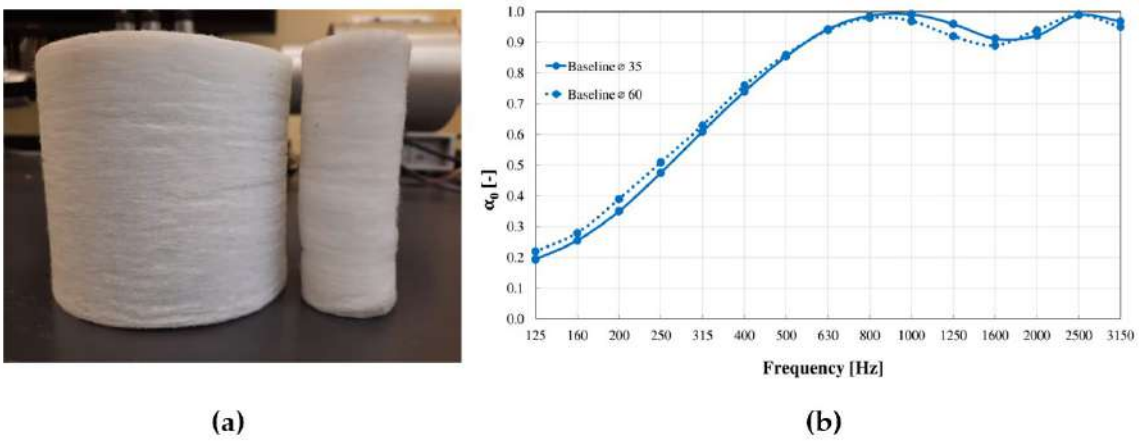

Figure 9. (**a**) Baseline polyester fiber sample with a density of 29 kg/m^3 and a thickness of 85 mm and (**b**) comparative measurements of the sound absorption coefficient of the baseline material.

3.2. Effect of the Sample Thickness

The graphs in Figure 10 plot the normal incidence sound absorption coefficient (α_0) in one-third-octave-band center frequencies of the tested samples, i.e., 60 mm samples in IT_{60} and 35 mm samples in IT_{35}. The plotted data were calculated as the arithmetic average of the results of three repeated measurements and presented a sound absorption coefficient, versus frequency, with a succession of peaks and troughs. As expected, the samples with the greater thickness (i.e., A1, B1, C1, D1, and eE1, with a thickness of 70 mm) performed better than the lower thickness samples (i.e., A2, B2, C2, D2, and E2, with a thickness of 50 mm) in the lower frequency range. This well-known trend has also been reported in previous studies investigating the sound absorption properties of 3D-printed materials in an impedance tube, such as [9,24]. In addition to the frequency shift, for a given sample tested in IT_{60} or IT_{35}, the peak absorption values are often comparable for the 70 mm and 50 mm thick samples, with α_0 values from 0.6 to 0.7 for IT_{60} (60 mm samples) and from 0.7 to 0.9 for IT_{35} (35 mm samples). The peak values, due to the first frequency of resonance of the porous material (i.e., quarter-wavelength $f_0 = c/4d$, where c = 343.1 m/s at 20 °C and d equals the material thickness), are generally observed in the range between 630 and 1000 Hz, in the case of the 70 mm thick samples, and the range between 800 and 1250 Hz, in the case of the 50 mm thick ones. Interestingly, these frequencies are almost half the amplitude of those expected from the f_0 formulation provided above (i.e., 1250–1600 and 2000–2500 for the 70 mm and 50 mm thicknesses, respectively). This is similar to the effect of coupling perforated panels and Helmholtz resonators with porous materials [26].

Further evidence of the effect of the top hard coating has been shown in the measurements (e.g., C2_2T vs. C2_2F) in

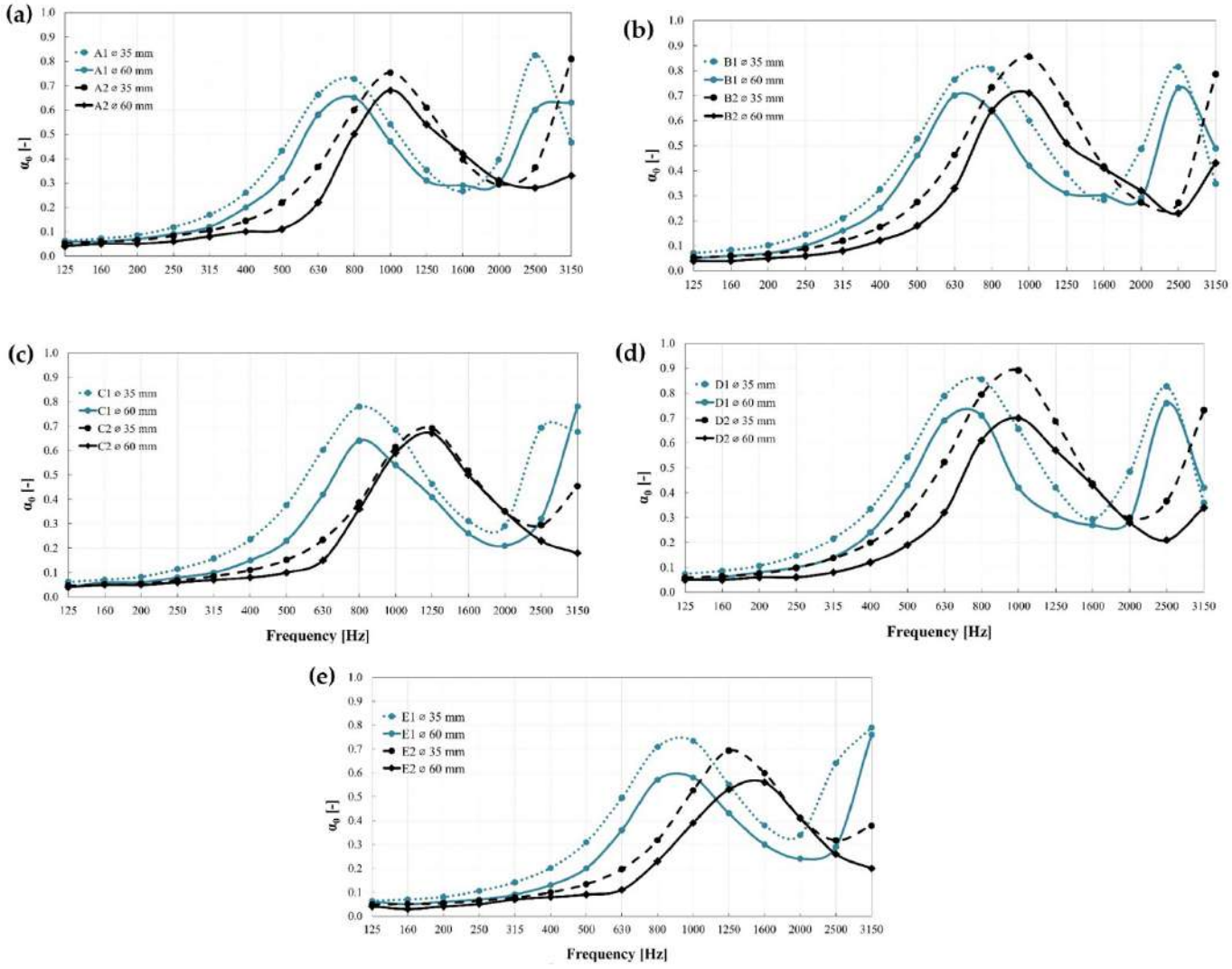

Figure 10. Normal incidence sound absorption coefficient of 60 mm samples and 35 mm samples, measured in IT_{60} and IT_{35}, respectively: (**a**) A1 and A2; (**b**) B1 and B2; (**c**) C1 and C2; (**d**) D1 and D2; and (**e**) E1 and E2.

Appendix D. The samples' foam core open areas (i.e., LCOAs) are vertical and interact with the sound waves mainly laterally and due to the back reflection over the TCOAs. The effect of surface roughness and impedance changes is to generate diffraction, i.e., the breaking up of sound wavefronts due to edges and other effects. The diffraction from the edges at low frequencies causes the reflected wave to no longer be planar, and so the simple theories (see the f_0 formulation above) no longer apply. As sound velocity is lower in the porous absorbents than in the air, HAMs also have the ability to perturb the sound field more at lower frequencies, when compared to hard diffusers of the same depth. In theory, HAMs can produce diffuse reflections at lower frequencies, although at low frequencies the effect of these materials can be dominated by absorption. This shows that the HAMs are behaving like the Helmholtz absorbers. The amount of added mass in the holes determines the increase in absorption at low frequencies [26]. The diffuse reflections could also be optimized at an early design stage, allowing for a more comprehensive study of the combined effect [33]. The effect of non-planar materials in impedance tube measurements has been investigated in past works [34], showing that, due to the shape

of the sample surface, the reflected pressure is not constant, varying from one point to another, and, consequently, the acoustic reflection coefficient is not well defined. The results showed that the first maximum peak is maintained and that the irregular steps smoothen the minima of the acoustic absorption. The first maximum remains unaltered for different configurations while the higher frequencies are subject to significant differences. To investigate this in a deeper way, the implementation of a more exact theoretical model to match the experimental results would be necessary.

The 1600–2000 Hz and 2000–2500 Hz troughs for the 70 mm and 50 mm thick samples, respectively, demonstrate a decremental trend of the sound absorption coefficient for all of them, regardless of the various configurations. It is possible to hypothesize that the visco-thermal losses that take place within the material are not sufficient to completely absorb the sound wave at these specific wavelengths. It can be assumed that the curves are little correlated above these frequencies (however within the accurate frequency range for both tubes), due to a more prevalent effect of the diffusive elements. As indicated in Section 2.1, at high frequencies, the hard parts of the sample reflect sound, causing a reduction in the absorption coefficient [26]. It is at these high frequencies, where the absorption is reduced, that the surface would disperse the reflected sound. However, as reported above, sound diffusion has not been further investigated in the present work.

3.3. Effect of the Sample Diameter

The comparison of the results obtained with the two impedance tubes showed a good level of agreement between the results obtained for 60 mm samples and 35 mm samples, as the frequencies of the peak absorption values were generally coherent for all samples. This trend could be justified by the comparable open areas (i.e., upper irregular reliefs) of both 60 mm samples and 35 mm samples being almost equal, regardless that the TCOAs of 60 mm samples are larger (see Appendix B, Table A2), indicating a good level of similarity between the two sets of samples and, therefore, representativeness criterion fulfillment. However, the sound absorption coefficients reported were systematically lower in the case of 60 mm samples than in 35 mm samples, with differences up to ∼0.15 at peaks. As mentioned in Section 2.1, the hybrid surfaces behave like Helmholtz absorbers (see also Appendix D). An approximation to the model of the slotted absorbers, which are a derivation of the Helmholtz absorbers, could have been made in the design phase. A simple model could be used, as implemented in [30], based on the theory developed in [26]. As reported in Section 2.1, the model requires data on airflow resistivity, top coating thickness, slot width, porous material thickness, and open area. The model could have been used to investigate the theoretical effect that airflow resistivity might have for fixed open areas (this is the case for each typology, see Appendix B, Table A2) and vice versa, adapting the model implemented in [30]. A limitation of this study is that it was not possible to perform air flow resistivity measurements to characterize the core foam for each sample. Based on this, the above-mentioned model could not be applied in this study. Nonetheless, the decrease in the airflow resistivity between samples would lead to a decrease in the absorption coefficient maintaining the same frequency peak, while variations in the open area would cause a decrease and a frequency shift of the frequency peak. Therefore, the differences in the peak values between the 60 mm samples and 35 mm samples could be attributed to any variation in the above-mentioned properties (e.g., air flow resistivity) due to any small differences in the 3D printing. In the literature, small differences in peak absorption values were also found in [25] between samples with different diameters (40, 30, and 29 mm) manufactured with the same AM technology and tested in independent labs. Given that previous studies [35] have found good agreements between measurements on the rather small and inhomogeneous sample, in the standing wave tube with a circular cross-section, and results using the transfer matrix method presupposing layers of infinite size, we assumed no artifacts induced by the tube walls. Further investigations through measurements on bigger samples (e.g., using the reverberation room method) could be

made and compared to the impedance tube measurements, and the implementation of more exact theories to match the experimental results would also be necessary.

3.4. Effect of the Sample Typology

For the sake of simplicity, the measured results have also been plotted in Figure 11, for the two samples' diameters separately, by grouping the samples based on the dimensions of the Truchet tile pattern on the panels' surfaces, i.e., samples B and D, exhibiting a tile side length of 20 mm, and A, C, and E with a tile side length of 40 mm. This was completed in an attempt to better shed light on the influence of the number of steps (see Sections 2.1 and 2.3, and Appendix D) on the measurement results obtained for a given Truchet tile size of the superficial pattern.

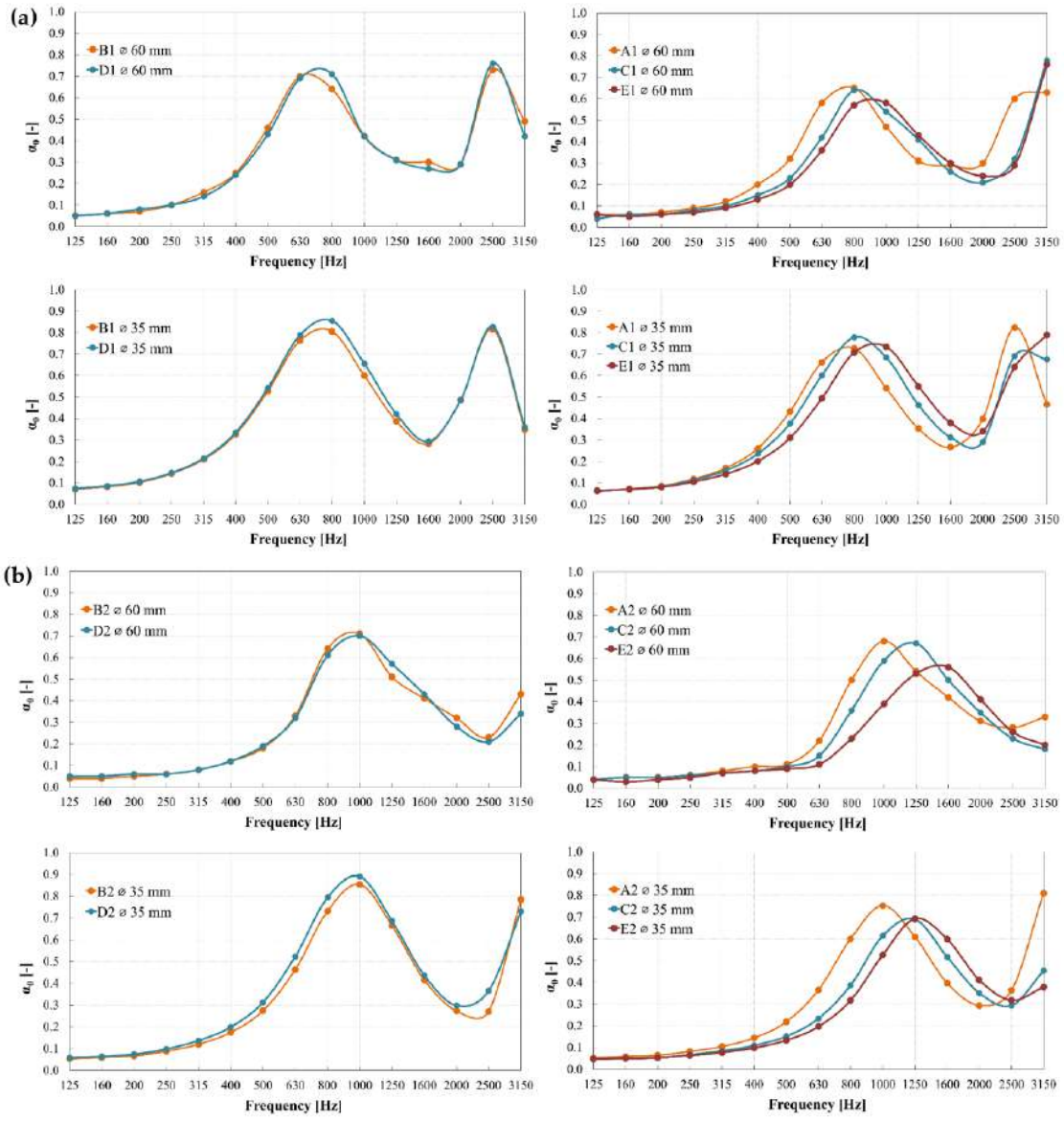

Figure 11. Normal incidence sound absorption coefficient of (**a**) the 70 mm thick samples; (**b**) the 50 mm thick samples. The results are grouped based on the side dimensions of the Truchet tiles, i.e., B and D, with a side length of 20 mm, and A, C, and E with a side length of 40 mm, and are shown separately for 60 mm samples (above) and 35 mm samples (below).

When comparing the B and D samples, having a tile side of 20 mm and 1 or 2 steps, respectively, the results were quite comparable, showing slightly lower values of the sound

absorption coefficient in the case of B samples (i.e., 1 step). As concerns the A, C, and E samples, with a side of 40 mm and 1, 2, or 3 steps, respectively, the results highlighted a shift in the peak absorption towards the higher frequencies for an increasing number of steps, since it resulted in a reduced thickness of the foam core. This finding aligns with the typical behavior of porous materials [26]. Despite the frequency shift, the peak absorption values were quite similar, with variations generally in the range of ± 0.1. From Figure 11 and Table 3 (see Section 2.3), it can be assumed that the volume difference (i.e., B1–D1, B2–D2, A1–C1, [. . .], and C2–E2) between the two sets (ranging from 1200 mm^3 to 3600 mm^3 for samples B and D, and from 3000 mm^3 to 7000 mm^3 for samples A, C, and E) is not the cause of the shifting pattern observed for samples A, C, and E. On the other hand, the Truchet tile side length of 40 mm, in conjunction with a step size larger than 8 mm, and an increasing number of steps seems to be the apparent cause.

4. Conclusions and Outlook

The sound-absorbing performance investigation of the customizable 3D-printed HAMs was presented in this contribution, demonstrating their potential through compilation. The proposed design methodology paves the way to a customizable large-scale cumulative acoustic performance by means of variable patterned stepped thickness. The challenges associated with the characterization of these materials through the impedance tube method have been explored considering the need to adequately represent the surface irregularities within the dimensional constraints of the two tube diameters. The results of the normal incidence sound absorption were collected and presented from ten configurations of a 3D-printed material and tested in two different measurement set-ups. The effect of the sample orientation, the sample diameter, and the sample typology were taken into consideration. The main results can be summarized as follows:

- The preliminary analysis in two orientations (i.e. at 0° and 90°) demonstrated an almost perfect overlapping between the measured data, suggesting that the orientation of the sample's irregularities within the impedance tube does not affect the measurement repeatability.
- The results obtained with the two impedance tubes demonstrated a good level of agreement on the first frequency of resonance, while at higher frequencies, larger differences occurred due to the non-plane wave propagation being affected by the surface irregularities and impedance variations.
- The HAMs performed better at lower frequencies than expected and behaved like Helmholtz absorbers, demonstrating a frequency shift pattern related to superficial geometric features, i.e., surface irregularities, compared to the theoretical frequency of resonance due to the material thickness alone.
- Lower values of sound absorption for the 60 mm diameter tube were observed at the frequency of resonance, suggesting a significant effect on the sample air volume (increasing factor of ~2.9).
- A shifting pattern in the peak absorption values towards higher frequencies was observed for specimens with a larger (i.e., 40 mm) Truchet tile size length, a step size larger than 8 mm, and a gradually incremental (i.e., 1, 2, and 3) number of steps. This suggests that a full frequency range acoustic absorber could be achieved by determining the proper combination of the design factors.

Future studies will focus on flow resistivity measurements to support the data presented, as well as on the analysis of the random incidence sound absorptive and diffusing properties of the material typologies, for large-scale performance-driven combinations. Furthermore, it might be worth considering different topological complexities with various combinations of porosity characteristics for the foam core (e.g., pore-size variations or unit cell typologies based on various Triply Periodic Minimal Surfaces (TPMS)) as well as different inclinations of the steps' walls. This last design parameter might significantly affect the activation of the sound-absorbing foam layer. Additionally, it might be interesting to consider the selective application of omni-phobic products for the introduction of self-

cleaning properties, enhanced durability, and, thus, an expanded lifespan. Furthermore, acoustic simulations based on FEM methods could be used after calibration based on the measured data achieved here. A more detailed parametric study could also be easily implemented and useful to explore design factors based on the fabrication and measurements set-ups limits.

Author Contributions: Conceptualization, V.T. and L.S.; methodology, V.T. and L.S.; formal analysis, V.T., L.S. and E.B.; investigation, V.T., L.S. and E.B.; resources, V.T. and A.K.; data curation, V.T., L.S. and E.B.; writing—original draft preparation, V.T., L.S. and E.B.; writing—review and editing, A.K. and A.A.; visualization, V.T. and E.B.; supervision, L.S.; project administration, V.T. and L.S. All authors have read and agreed to the published version of the manuscript.

Funding: The experimental activities presented in this paper were carried out as part of the H2020 project "iclimabuilt—Functional and advanced insulating and energy harvesting/storage materials across climate adaptive building envelopes" (Grant Agreement no. 952886).

Data Availability Statement: Data are available upon request.

Acknowledgments: We thank Efstratios Kroustis (Mechanical Engineer, BioG3D) for the technical support of the project.

Conflicts of Interest: The authors declare no conflict of interest.

Appendix A

Table A1. Typical material properties of colorFabb Light-Weight PLA (LW PLA): 3D-printed and injection molded [32].

Physical Properties	Unit	Value at 200 °C; 100% Flow	Value at 250 °C; 45% Flow	Method
Tensile modulus	MPa	3333.76	864.25	ISO 527
Yield strength	MPa	43.07	N/A	ISO 527
Yield strain	%	1.68	N/A	ISO 527
Tensile strength	MPa	43.07	10.83	ISO 527
Tensile strain at tensile strength	%	1.68	12.00	ISO 527
Tensile stress at break	MPa	38.74	10.73	ISO 527
Tensile strain at break	%	8.08	12.78	ISO 527
Charpy unnotched impact strength	kJ/m^2		5.46	ISO 179-1/1 eU
Charpy notched impact strength	kJ/m^2		3.67	ISO 179-1/1 eU
Density	kg/m^3	400–1240		
Glass transition Temperature	°C	55–60		DSC

Appendix B

Table A2. Interdependencies of TCOAs and LCOAs for the five upper surface design typologies.

	Acoustic Panel		**Sample 60 mm**		**Sample 35 mm**	
Profile Type	**Rectangular**		**Circular**		**Circular**	
Visual Representation						
Size (mm)	L160 × W160 × **H70**	L160 × W160 × **H50**	Ø60 × **H70**	Ø60 × **H50**	Ø35 × **H70**	Ø35 × **H50**

Table A2. *Cont.*

	Acoustic Panel		**Sample 60 mm**		**Sample 35 mm**	
Profile Type	**Rectangular**		**Circular**		**Circular**	
TTA (mm^2)	25,600		2827		935	
$TTA_{60\ mm}$: $TTA_{35\ mm}$				3.02		
TTA% (%)	100		100		100	
$TTA\%_{60\ mm}$: $TTA\%_{35\ mm}$				1.00		
	A1	**A2**	**A1**	**A2**	**A1**	**A2**
Visual Representation						
TCOA (mm^2)	13,404		1371		655	
$TCOA_{60\ mm}$: $TCOA_{35\ mm}$				**2.09**		
TCOA% (%)	52.36		48.50		70.05	
$TCOA\%_{60\ mm}$: $TCOA\%_{35\ mm}$				**0.69**		
LCOA (mm^2)	26,808		2680		1197	
$LCOA_{60\ mm}$: $LCOA_{35\ mm}$				**2.24**		
Open Area (LCOA/LCOA + TCOA) (mm^2)	0.67		**0.66**		**0.65**	
	B1	**B2**	**B1**	**B2**	**B1**	**B2**
Visual Representation						
TCOA (mm^2)	13,404		1543		547	
$TCOA_{60\ mm}$: $TCOA_{35\ mm}$				**2.82**		
TCOA% (%)	52.36		54.58		58.5	
$TCOA\%_{60\ mm}$: $TCOA\%_{35\ mm}$				**0.93**		
LCOA (mm^2)	26,808		3072		1074	
$LCOA_{60\ mm}$: $LCOA_{35\ mm}$				**2.86**		
Open Area (LCOA/LCOA + TCOA) (mm^2)	0.67		**0.67**		**0.66**	

Table A2. *Cont.*

	Acoustic Panel		**Sample 60 mm**		**Sample 35 mm**	
Profile Type	**Rectangular**		**Circular**		**Circular**	
	C1	**C2**	**C1**	**C2**	**C1**	**C2**
Visual Representation						
TCOA (mm^2)	21,726		2289		801	
$TCOA_{60\ mm}$: $TCOA_{35\ mm}$				**2.86**		
TCOA% (%)	84.87		80.97		85.67	
$TCOA\%_{60\ mm}$: $TCOA\%_{35\ mm}$				**0.95**		
LCOA (mm^2)	32,261		3503		1209	
$LCOA_{60\ mm}$: $LCOA_{35\ mm}$				**2.90**		
Open Area (LCOA/LCOA + TCOA) (mm^2)	0.60		**0.60**		**0.60**	
	D1	**D2**	**D1**	**D2**	**D1**	**D2**
Visual Representation						
TCOA (mm^2)	21,726		2452		835	
$TCOA_{60\ mm}$: $TCOA_{35\ mm}$				**2.94**		
TCOA% (%)	84.87		86.74		89.3	
$TCOA\%_{60\ mm}$: $TCOA\%_{35\ mm}$				**0.97**		
LCOA (mm^2)	32,261		3589		1167	
$LCOA_{60\ mm}$: $LCOA_{35\ mm}$				**3.08**		
Open Area (LCOA/LCOA + TCOA) (mm^2)	0.60		**0.59**		**0.58**	
	E1	**E2**	**E1**	**E2**	**E1**	**E2**
Visual Representation						
TCOA (mm^2)	23,667		2577		814	
$TCOA_{60\ mm}$: $TCOA_{35\ mm}$				**3.17**		

Table A2. *Cont.*

	Acoustic Panel	Sample 60 mm	Sample 35 mm
Profile Type	**Rectangular**	**Circular**	**Circular**
TCOA% (%)	92.45	91.16	87.06
$TCOA\%_{60\ mm}$: $TCOA\%_{35\ mm}$		**1.05**	
LCOA (mm^2)	38,180	4163	1388
$LCOA_{60\ mm}$: $LCOA_{35\ mm}$		**3.00**	
Open Area (LCOA/LCOA + TCOA) (mm^2)	0.62	**0.62**	**0.63**

Appendix C

The preliminary test was carried out in the IT_{35} on samples A1 and C1 since, in both cases, the test samples presented inhomogeneous surface patterns with a good level of symmetry. For each sample, two measurements were compared, one with a given sample orientation within the tube, identified as "0°", and the other one with the sample rotated by ~90°, identified as "90°". The two sample positions inside IT_{35} are shown in Figure A1.

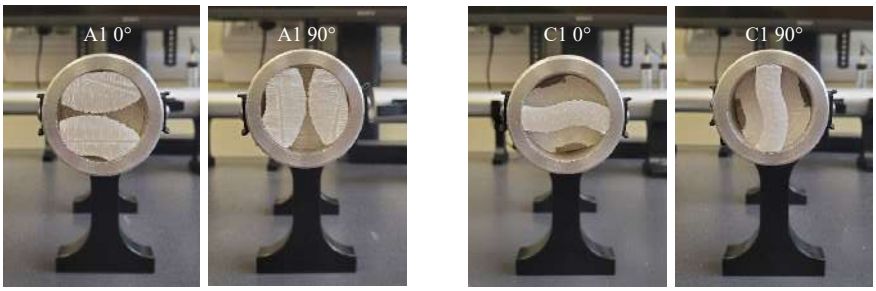

Figure A1. Pictures of the A1 and C1 samples with the two orientations, i.e., 0° and 90°, inside IT_{35}.

The results of the preliminary investigation on the influence of the samples' orientation on the measurement results are shown in Figure A2. As it can be noticed, there is an almost perfect overlapping between the measured data obtained for the two orientations, i.e., at 0° and 90°, suggesting that the orientation of the sample within the impedance tube does not affect the measurement repeatability.

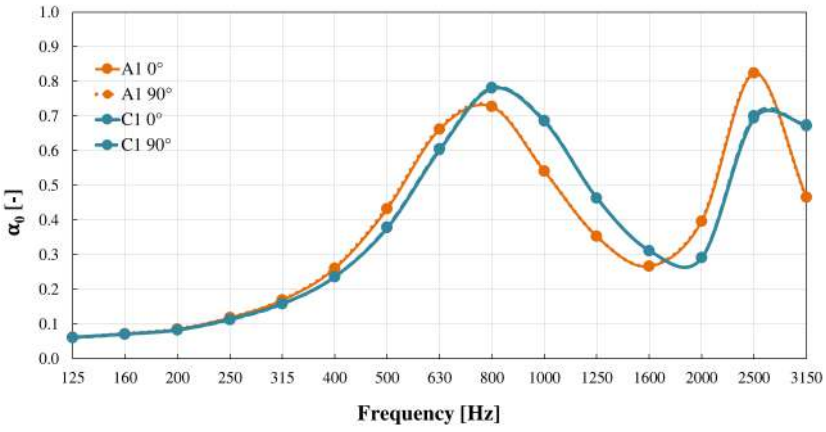

Figure A2. Sound absorption coefficients of samples A1 and C1 with either a 0° or 90° orientation within IT_{35}.

Appendix D

The tested sample C2 is composed of a foam core and an irregular structure on top of it forming three steps of top coating indicated as 3T in the denominations of the samples. As indicated in Section 2.2, the foam core is a customized structure based on a gyroid pattern. The top surfaces were printed as a compact layer (infill pattern of 100% density) of 2 mm thickness. It should be noted that each top coating step has been indicated as 3T, 2T, and T; the foam steps have been indicated as 3F, 2F, and F. All tested samples were obtained by cutting each step progressively.

The results of the measurements of the one-third-octave band's sound absorption coefficients are presented in Figure A3.

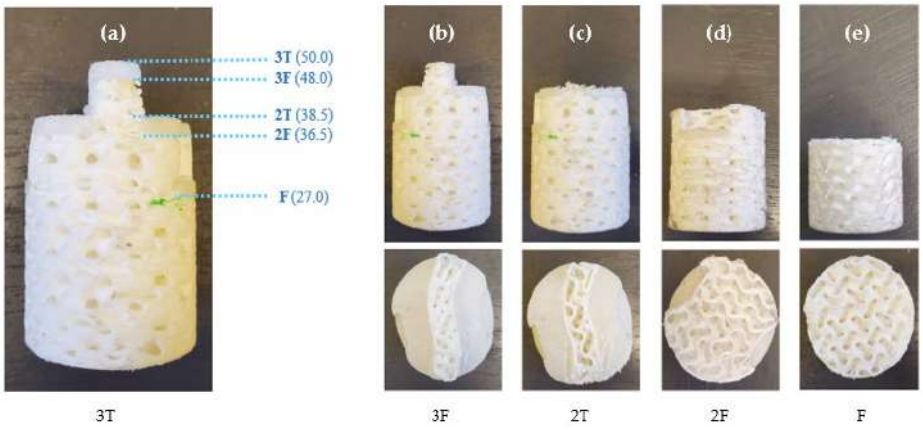

Figure A3. Progressive transformation of the C2 sample for ISO 10534-2:2001 measurements on (**a**) C2_3T (data in brackets show the thickness of the sample at each step); (**b**) C2_3F; (**c**) C2_2T; (**d**) C2_2F; and (**e**) C2_F.

The effect of the foam core of the first step (the upper one) could be observed by comparing samples C2_3T with C2_3F (Figure A4). The differences between the results of the two samples were quite small and the effect of the first top coating layer is very limited. For the second top coating step, i.e., the middle one, the effects could be observed by comparing C2_2T with C2_2F (Figure A4). In this case, it was shown that the differences were more evident as shifts in both the maxima and minima. Given these shifts, the values of the sound absorption were lower, up to 1600 Hz for the C2_2F sample, and were higher for the range 1600–3150 Hz. Moreover, comparing the curves presented in Figure A4 for C2_3F and C2_3T, it can be observed that there was a shift toward lower frequencies (from 2000 Hz to 1250 Hz) and an approximate increment of the sound absorption coefficient from 0.5 up to 0.7.

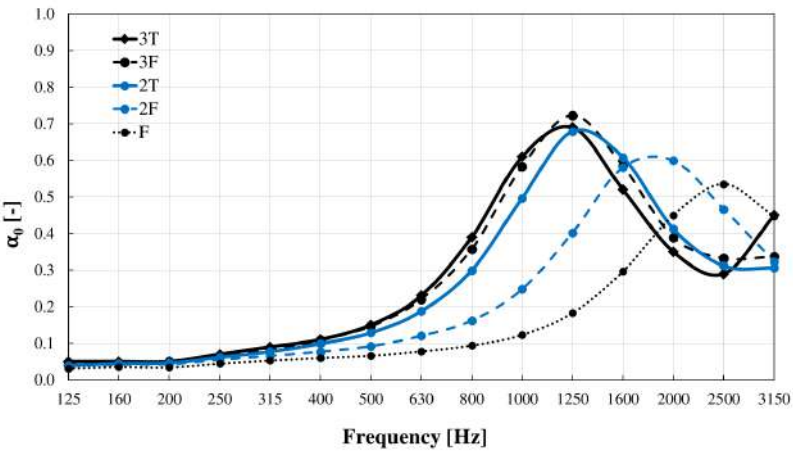

Figure A4. Sound absorption coefficients of samples C2_3T, C2_3F, C2_2T, C2_2F, and C2_F.

References

1. Badino, E.; Shtrepi, L.; Astolfi, A. Acoustic Performance-Based Design: A Brief Overview of the Opportunities and Limits in Current Practice. *Acoustics* **2020**, *2*, 246–278. [CrossRef]
2. Kuttruff, H. *Room Acoustics*, 6th ed.; Routledge: London, UK, 2016. [CrossRef]
3. World Health Organization. *Regional Office for Europe. Combined or Multiple Exposure to Health Stressors in Indoor Built Environments: An Evidence-Based Review Prepared for the WHO Training Workshop "Multiple Environmental Exposures and Risks", Bonn, Germany, 16–18 October 2013*; World Health Organization: Geneva, Switzerland, 2013.
4. Itard, L.; Meijer, F.; Vrins, E.; Hoiting, H. *Building Renovation and Modernisation in Europe: State of the Art Review*; OTB Research Institute for Housing, Delft University of Technology: Delft, The Netherlands, 2008.
5. Paoletti, I. Mass Customization with Additive Manufacturing: New Perspectives for Multi Performative Building Components in Architecture. *Procedia Eng.* **2017**, *180*, 1150–1159. [CrossRef]
6. Islam, S.; Bhat, G.; Sikdar, P. Thermal and Acoustic Performance Evaluation of 3D-Printable PLA Materials. *J. Build. Eng.* **2023**, *67*, 105979. [CrossRef]
7. Žujović, M.; Obradović, R.; Rakonjac, I.; Milošević, J. 3D Printing Technologies in Architectural Design and Construction: A Systematic Literature Review. *Buildings* **2022**, *12*, 1319. [CrossRef]
8. Prasittisopin, L.; Pongpaisanseree, K.; Jiramarootapong, P.; Snguanyat, C. Thermal and Sound Insulation of Large-Scale 3D Extrusion Printing Wall Panel. In Proceedings of the 2nd RILEM International Conference on Concrete and Digital Fabrication, Eindhoven, The Netherlands, 6–8 July 2020; Springer: Berlin/Heidelberg, Germany, 2020; Volume 28, pp. 1174–1182. [CrossRef]
9. Vasina, M.; Monkova, K.; Pavol Monka, P.; Kozak, D.; Tkac, J. Study of the Sound Absorption Properties of 3D-Printed Open-Porous ABS Material Structures. *Polymers* **2020**, *12*, 1062. [CrossRef] [PubMed]
10. Boulvert, J.; Cavalieri, T.; Costa-Baptista, J.; Schwan, L.; Romero-García, V.; Gabard, G.; Fotsing, E.R.; Ross, A.; Mardjono, J.; Groby, J.P. Optimally Graded Porous Material for Broadband Perfect Absorption of Sound. *J. Appl. Phys.* **2019**, *126*, 175101. [CrossRef]
11. Liu, Z.; Zhan, J.; Fard, M.; Davy, J.L. Acoustic Properties of a Porous Polycarbonate Material Produced by Additive Manufacturing. *Mater. Lett.* **2016**, *181*, 296–299. [CrossRef]
12. Attenborough, K. Macro- and Micro-Structure Designs for Porous Sound Absorbers. *Appl. Acoust.* **2019**, *145*, 349–357. [CrossRef]
13. Cai, X.; Guo, Q.; Hu, G.; Yang, J. Ultrathin Low-Frequency Sound Absorbing Panels Based on Coplanar Spiral Tubes or Coplanar Helmholtz Resonators. *Appl. Phys. Lett.* **2014**, *105*, 121901. [CrossRef]
14. Attenborough, K. Microstructures for Lowering the Quarter Wavelength Resonance Frequency of a Hard-Backed Rigid-Porous Layer. *Appl. Acoust.* **2018**, *130*, 188–194. [CrossRef]
15. Liu, Z.; Zhan, J.; Fard, M.; Davy, J.L. Acoustic Properties of Multilayer Sound Absorbers with a 3D Printed Micro-Perforated Panel. *Appl. Acoust.* **2017**, *121*, 25–32. [CrossRef]
16. Huang, W.; Schwan, L.; Romero-García, V.; Génevaux, J.M.; Groby, J.P. 3D-Printed Sound Absorbing Metafluid Inspired by Cereal Straws. *Sci. Rep.* **2019**, *9*, 8496. [CrossRef] [PubMed]
17. Casarini, C.; Tiller, B.; Mineo, C.; MacLeod, C.N.; Windmill, J.F.C.; Jackson, J.C. Enhancing the Sound Absorption of Small-Scale 3D Printed Acoustic Metamaterials Based on Helmholtz Resonators. *IEEE Sens. J.* **2018**, *18*, 7949–7955. [CrossRef]
18. Setaki, F.; Tian, F.; Turrin, M.; Tenpierik, M.; Nijs, L.; Van Timmeren, A. 3D-Printed Sound Absorbers: Compact and Customisable at Broadband Frequencies. *Archit. Struct. Constr.* **2023**, *3*, 205–215. [CrossRef]
19. Setaki, F.; Tenpierik, M.; Timmeren, A.V.; Turrin, M. New Sound Absorption Materials: Using Additive Manufacturing for Compact Size, Broadband Sound Absorption at Low Frequencies. In Proceedings of the Inter-Noise 2016, Hamburg, Germany, 21–24 August 2016.
20. Sekar, V.; Eh Noum, S.Y.; Putra, A.; Sivanesan, S.; Chin Vui Sheng, D.D. Fabrication of Light-Weighted Acoustic Absorbers Made of Natural Fiber Composites via Additive Manufacturing. *Int. J. Lightweight Mater. Manuf.* **2022**, *5*, 520–527. [CrossRef]
21. Yang, W.; Bai, X.; Zhu, W.; Kiran, R.; An, J.; Chua, C.K.; Zhou, K. 3D Printing of Polymeric Multi-Layer Micro-Perforated Panels for Tunable Wideband Sound Absorption. *Polymers* **2020**, *12*, 360. [CrossRef]
22. Jiang, C.; Moreau, D.; Doolan, D. Acoustic Absorption of Porous Materials Produced by Additive Manufacturing with Varying Geometrics. In Proceedings of the AAS2017 Acoustics 2017 Perth: Sound, Science and Society, Perth, Australia, 19–22 November 2017.
23. Aslan, R.; Turan, O. Gypsum-Based Sound Absorber Produced by 3D Printing Technology. *Appl. Acoust.* **2020**, *161*, 107162. [CrossRef]
24. Monkova, K.; Vasina, M.; Monka, P.P.; Vanca, J.; Kozak, D. Effect of 3D-Printed PLA Structure on Sound Reflection Properties. *Polymers* **2022**, *14*, 413. [CrossRef]
25. Zieliński, T.G.; Opiela, K.C.; Pawłowski, P.; Dauchez, N.; Boutin, T.; Kennedy, J.; Trimble, D.; Rice, H.; Van Damme, B.; Hannema, G.; et al. Reproducibility of Sound-Absorbing Periodic Porous Materials Using Additive Manufacturing Technologies: Round Robin Study. *Addit. Manuf.* **2020**, *36*, 101564. [CrossRef]
26. Cox, T.J.; D'Antonio, P. *Acoustic Absorbers and Diffusers: Theory, Design and Application*, 3rd ed.; Taylor & Francis: Abingdon-on-Thames, UK, 2017.
27. *ISO/IEC 17025:2017*; General Requirements for the Competence of Testing and Calibration Laboratories. International Organization for Standardization: Geneva, Switzerland, 2017.

28. *ISO 10534-2:2001*; Acoustics: Determination of Sound Absorption Coefficient and Impedance in Impedance Tubes. Part 2, Transfer-Function Method. International Organization for Standardization: Geneva, Switzerland, 2001.
29. Smith, C.S.; Boucher, P. The Tiling Patterns of Sebastien Truchet and the Topology of Structural Hierarchy. *Leonardo* **2017**, *20*, 373–385. [CrossRef]
30. Cox, T.J. Modelling of Acoustic Absorbers: Predict Material Properties, Surface Impedance and Absorption Coefficients of Acoustic Absorbers. Available online: https://www.mathworks.com/matlabcentral/fileexchange/54004-modelling-of-acoustic-absorbers?tab=discussions (accessed on 5 July 2023).
31. Buj-Corral, I.; Bagheri, A.; Domínguez-Fernández, A.; Casado-López, R. Influence of Infill and Nozzle Diameter on Porosity of FDM Printed Parts with Rectilinear Grid Pattern. *Procedia Manuf.* **2019**, *41*, 288–295. [CrossRef]
32. colorFabb LW-PLA—Technical Datasheet. Available online: https://colorfabb.com/media/datasheets/tds/colorfabb/TDS_E_ColorFabb_LW-PLA.pdf (accessed on 11 July 2023).
33. Shtrepi, L.; Mendéz Echenagucia, T.; Badino, E.; Astolfi, A. A Performance-Based Optimization Approach for Diffusive Surface Topology Design. *Build. Acoust.* **2021**, *28*, 231–247. [CrossRef]
34. Pfretzschner, J.; Simon, F.; Rodriguez, R.M.; de la Colina, C. Simplified Calculus to Estimate the Acoustical Absorption of Nonplanar Materials. *J. Acoust. Soc. Am.* **1999**, *105*, 1316. [CrossRef]
35. Kristiansen, U.R.; Vigran, T.E. On the Design of Resonant Absorbers Using a Slotted Plate. *Appl. Acoust.* **1994**, *43*, 39–48. [CrossRef]

Disclaimer/Publisher's Note: The statements, opinions and data contained in all publications are solely those of the individual author(s) and contributor(s) and not of MDPI and/or the editor(s). MDPI and/or the editor(s) disclaim responsibility for any injury to people or property resulting from any ideas, methods, instructions or products referred to in the content.